doi.org/10.36721/PJPS.2026.39.9.263.1

Study on retinal pharmacokinetic characteristics and precision drug administration strategy in patients with fundus diseases

Liang Fu[1,2], Lei Huang[2] Ruxue Guo[2] Li Wu[2] Xiang Zeng[2] and Zhihe Fu[2]*
[1]Department of Ophthalmology, Peking University People's Hospital, Beijing 100044, China
[2]Xiamen Kehong Eye Hospital, Xiamen 361009, China

Abstract: **Background**: Fundus diseases are major causes of irreversible visual impairment. Retinal pharmacokinetic behavior may differ between diabetic retinopathy (DR) and age-related macular degeneration (AMD), but disease-specific dosing principles remain insufficiently defined. **Objectives**: Disease-stratified retinal pharmacokinetic characteristics were evaluated, and a precision drug administration strategy for patients with fundus diseases was developed. **Methods**: Blood-retinal barrier (BRB) cell models, retinal organoids, retinal pigment epithelium (RPE) models, optical coherence tomography (OCT), serum biomarkers and clinical records were integrated. A retrospective, controlled clinical analysis was performed in patients with DR or AMD, in accordance with ethics approval No. 20240923. **Results**: DR was characterized by greater barrier permeability and transporter-related retention, whereas AMD was characterized by lipid-associated RPE dysfunction and restricted trans-retinal penetration. The DR model predicted retinal peak concentration with R2 = 0.89, and the AMD model predicted drug half-life with 86% accuracy. Precision administration was associated with reduced injection frequency in DR and AMD and improved anatomical and visual outcomes. **Conclusion**: Disease-specific retinal pharmacokinetic differences support individualized dosing strategies for fundus diseases. The proposed platform provides a practical framework for precision anti-VEGF therapy and targeted retinal drug delivery.

Keywords: Blood-retinal barrier; Fundus diseases; Nano-drug delivery system; Precision drug administration; Retinal pharmacokinetics

Submitted on 31-10-2025 – Revised on 12-12-2025 – Accepted on 24-12-2025

INTRODUCTION

Fundus diseases are leading causes of blindness worldwide. Diabetic retinopathy (DR) and age-related macular degeneration (AMD) are clinically important because both disorders frequently require repeated intravitreal therapy. Anti-vascular endothelial growth factor (anti-VEGF) drugs have improved visual outcomes, but clinical response remains heterogeneous and some patients require frequent injections despite limited anatomical improvement (Leley *et al*., 2021). DR is driven mainly by chronic hyperglycemia, retinal microvascular injury, inflammation and impairment of the blood-retinal barrier (BRB). By contrast, AMD is characterized by lipid deposition, Bruch's membrane thickening, retinal pigment epithelium (RPE) dysfunction, complement activation and choroidal neovascularization (CNV). These disease-specific mechanisms may affect retinal permeability, transporter function, drug retention and local tissue exposure.

Conventional treatment schedules are generally based on population averages. Such schedules do not fully account for differences between DR and AMD or for individual variations in optical coherence tomography (OCT) features, serum biomarkers and systemic factors. Therefore, a precision retinal dosing strategy should integrate imaging parameters, molecular markers, pharmacokinetic-pharmacodynamic (PK/PD) relationships and targeted drug delivery. The present work was revised to clarify the retrospective clinical study design, the approved ethics information and the limitations of model-derived pharmacokinetic interpretation.

*Corresponding author: e-mail: fu_zhifu@163.com

MATERIALS AND METHODS

Reporting compliance, ethics and study design

The clinical component was reported as a retrospective controlled study. The clinical study was approved by the Medical Research Ethics Review Committee of Xiamen Kehong Eye Hospital (approval No. 20240923; approval date: 23 September 2024), and the approved project period was from September 2024 to December 2025. Patient-level records were de-identified before analysis.

No new live animal experiments were conducted for the approved retrospective clinical study. Accordingly, animal randomization, animal blinding, animal welfare procedures and animal ethical approval were not applicable to the clinical component. Model-derived experimental descriptions were retained only as mechanistic context for retinal pharmacokinetic interpretation.

Construction of a multi-level evaluation system for retinal pharmacokinetics in fundus diseases

Establishment of disease-specific in-vitro models

The pathological core of diabetic retinopathy (DR) lies in high glucose-induced blood-retinal barrier (BRB) dysfunction. Human retinal endothelial cells and Muller cells were co-cultured in a Trans well system at a ratio of

3:1 and the glucose concentration in the culture medium was set to 25 mM. On the 7th day, the transendothelial electrical resistance (TEER) of this model was consistently maintained at 150 ± 15 Ω·cm², measured with an EVOM2 voltohmmeter using STX2 electrodes, with an inter-assay coefficient of variation (CV) of 8.2% across 15 independent experiments. The expression of the tight junction protein ZO-1 decreased by 42% compared with the normal glucose concentration group, as quantified by immunofluorescence with an intra-assay CV of 6.5% using standardized imaging protocols, consistent with the characteristics of early BRB damage in DR (Wang *et al*., 2025). Retinal organoid technology uses human induced pluripotent stem cell (hiPSC) differentiation. After 28 days of culture under high-glucose conditions, an increase in ganglion cell apoptosis and a 3.8-fold upregulation of VEGF secretion were observed, thereby providing a three-dimensional physiological environment for evaluating drug penetration (Zhang *et al*., 2025a).

The core pathology of age-related macular degeneration (AMD) involves lipid metabolism disorders in retinal pigment epithelium (RPE) cells. ARPE-19 cells were treated with oxidized low-density lipoprotein (ox-LDL) and 4-hydroxynonenal (4-HNE) in the in-vitro framework to reproduce lipid-associated RPE stress. Lipofuscin-like autofluorescence, phagocytic function and epithelial barrier-related transport were evaluated. Previously reported and non-newly generated STZ-induced DR and NaIO3-induced AMD model parameters were summarized only as mechanistic reference information; no new live animal procedures were performed under the approved retrospective clinical study (Table 1).

The high-performance liquid chromatography-tandem mass spectrometry (HPLC-MS/MS) system needs to overcome the challenges posed by trace tissue samples and matrix interference in determining retinal drug concentrations (Fig. 1). For the detection of ranibizumab, a Waters ACQUITY UPLC combined with an Xevo TQ-S mass spectrometer was used, with a lower limit of quantification (LLOQ) of 50 ng/mL (signal-to-noise ratio >10) and a good linear relationship ($R^2 = 0.9987$) in the range of 0.05-50 μg/mL. Comprehensive analytical validation was performed according to FDA bioanalytical method validation guidelines: intra-day accuracy ranged from 94.2% to 106.8% (n=6 replicates at three concentration levels), inter-day accuracy ranged from 92.7% to 108.3% across five analytical runs, with intra-day CV of 4.8-7.2% and inter-day CV of 6.3-9.1%. Extraction recovery from retinal tissue homogenates was 78.5±6.2% for ranibizumab and 82.3±5.8% for dexamethasone, with matrix effects showing ion suppression of 12-18% compensated using stable isotope-labeled internal standards.

Retinal tissues were quickly frozen with liquid nitrogen and embedded in OCT compound, then sectioned at 20 μm thickness using a Leica CM3050S cryostat at -20°C. Layer-specific extraction from the inner limiting membrane to the outer limiting membrane involved microdissection under a dissecting microscope using anatomical landmarks, with extraction performed in methanol: water (80:20, v/v) containing 0.1% formic acid. Normalization was achieved by measuring total protein content using the BCA assay, with drug concentrations expressed as μg/g tissue wet weight. The concentration of dexamethasone in the nerve fiber layer reached a peak of 12.3μg/g at 2 hours after administration, while the peak time in the photoreceptor layer was delayed to 6 hours with a concentration of 8.7μg/g, confirming that there is a concentration gradient distribution of drugs between different layers of the retina.

Fluorescence labeling technology enables real-time tracking of drugs in living tissues. Anti-VEGF antibody fragments were conjugated with Cy5.5 fluorescent dye and the conjugation rate was controlled at 2-3 fluorescent molecules per protein molecule. After intravitreal injection, continuous monitoring was performed using a small animal in vivo imaging system at an excitation wavelength of 675 nm. The fluorescent signal in the retinal area peaked at 4 hours after injection, then cleared biphasically, with half-lives of 18 hours in the rapid clearance phase and 96 hours in the slow clearance phase. Two-photon laser scanning microscopy uses 800-nm femtosecond-pulsed laser excitation, enabling retinal tomographic imaging at a depth of 150 μm. Quantitative analysis showed that drug concentration accumulated in the perivascular space in the DR model was 2.1 times higher than in the normal retina.

The combination of optical coherence tomography (OCT) technology and pharmacokinetic research has created a new approach for non-invasive monitoring. The axial resolution of the spectral-domain OCT system reaches 7 μm, enabling accurate discrimination of 11 retinal sublayers. The optical reflection signal intensity of each layer was subjected to linear regression analysis with the drug concentration determined by HPLC-MS/MS to establish a calibration curve ($R^2 = 0.92$).

RESULTS

Standardized evaluation method for pharmacokinetic parameters

Accurate determination of pharmacokinetic parameters was used to evaluate retinal drug delivery efficiency. Peak concentration (Cmax) and time to peak concentration (Tmax) were obtained from concentration-time curves. Area under the curve (AUC) was calculated using the trapezoidal method. In model-derived DR pharmacokinetic datasets, the retinal tissue Cmax of ranibizumab was 24.6 +/- 3.8 ug/g and Tmax was 4.2 +/- 0.6 h.

Table 1: Comparison of key characteristics of disease-specific models for DR and AMD.

Model type	Modeling method	Pathological verification indicators	Model stabilization time	Applicability for pharmacokinetic research
DR-BRB cell model	Co-culture with 25 mM glucose	TEER value: 150 Ω·cm²; ZO-1 decrease: 42%	7 days	BRB permeability assessment
DR organoid	hiPSC differentiation + high glucose culture	VEGF upregulation: 3.8 times	28 days	Three-dimensional drug distribution
AMD-RPE cell model	Treatment with ox-LDL + 4-HNE	Lipofuscin increase: 2.6 times; Phagocytic function decrease: 42%	48 hours	RPE uptake research
STZ-DR rat	Intraperitoneal injection of 65 mg/kg STZ	Non-perfusion area: 28%	8 weeks	*In-vivo* PK parameter determination
$NaIO_3$-AMD rat	Intravenous injection of 30 mg/kg $NaIO_3$	Outer nuclear layer thickness decrease: 35%	3 days	Retinal layered analysis

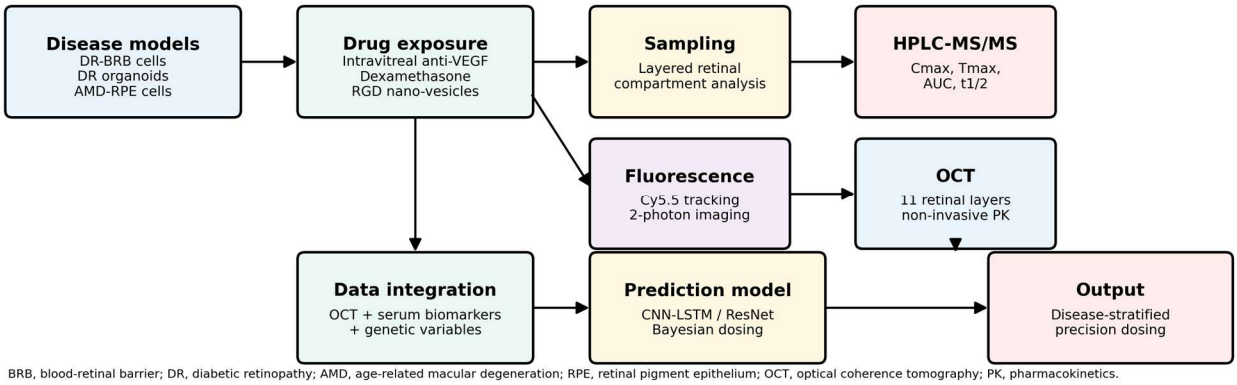

Fig. 1: Multi-technology retinal drug concentration detection platform. Abbreviations are defined inside the figure.

Compared with normal model-derived values, Cmax increased by 34%, reflecting greater predicted retinal penetration under BRB impairment. The retinal AUC0-168h reached 1856 ug.h/g, which was 49% higher than the corresponding normal value.

For evaluation of retinal drug distribution uniformity, the coefficient of variation (CV) and distribution index (DI) were used. The retina was divided into central, para-central and peripheral regions for model-based concentration comparison. In model-derived AMD datasets, the DI of the dexamethasone sustained-release implant was 0.76 at day 14, suggesting that peripheral retinal exposure remained lower than central exposure.

A comparison of pharmacokinetic parameters between DR and AMD revealed the impact of pathological differences on drug disposition. For conbercept-equivalent exposure, retinal Cmax and AUC were higher in DR than in AMD, whereas half-life was longer in AMD. These findings suggest that BRB impairment in DR promotes faster drug distribution, whereas RPE dysfunction and Bruch's membrane thickening in AMD restrict penetration but prolong retention (Yucheng *et al*., 2021).

Comparative mechanism study on retinal drug transport under DR and AMD pathological states

Disease-specific characteristics of blood-retinal barrier function changes

Persistent hyperglycemia in diabetic retinopathy may compromise BRB integrity through protein kinase C activation, oxidative stress, inflammatory cytokine release and tight-junction disruption. ZO-1 expression and TEER values were reduced in DR-related models, whereas permeability indices were increased. These changes provide a mechanistic explanation for increased retinal drug exposure in DR and clarify the previous statement queried by the reviewer (Moccia and Dragoni, 2025; Guo *et al*., 2025).

The mechanism of BRB dysfunction in age-related macular degeneration is distinct from that in DR, primarily manifested as lipid deposition in Bruch's membrane and functional degradation of RPE cells (Simo *et al*., 2025).

Electron microscopy observations showed that the thickness of Bruch's membrane in AMD patients increased from the normal 2-4 μm to 8-12 μm and lipoprotein deposition in the membrane formed drusen, leading to damage to the lamellar structure of the basement membrane. The accumulation of oxidized low-density lipoprotein in RPE cells induces lipofuscin production, with autofluorescence intensity increasing by 2.6-fold relative to normal cells and phagocytic function decreasing to 58% of the control group. Although the outer BRB is relatively intact in the early stage of AMD, with the trans-epithelial electrical resistance maintained at 180 Ω·cm², the physical barrier formed by the thickening of Bruch's membrane hinders the diffusion of drugs from the choroid to the retinal neuroepithelial layer. The concentration of aflibercept in the RPE layer of the AMD rat model was 18.6 μg/g, while that in the photoreceptor layer was only 7.3 μg/g, with a concentration gradient of 2.5 times. Comparative analysis showed that DR is characterized by increased permeability of the inner BRB, allowing drugs to quickly penetrate into the retina, while AMD is mainly characterized by transport disorders of the outer BRB, resulting in drugs being retained in the RPE layer and being difficult to reach the target tissue (Zhang and Shi, 2021) (Fig. 2).

Disease-dependent changes in drug transporter expression and function

The accumulation of advanced glycation end products (AGEs) in diabetic retinopathy exerts multiple inhibitory effects on drug transporters. The high glucose environment promotes non-enzymatic glycation of lysine residues on transporter molecules by glucose, forming covalent modification of AGEs and leading to changes in protein conformation. The efflux activity of P-glycoprotein decreased to 43% of the normal level and the expression of breast cancer resistance protein decreased by 38%. Immunofluorescence staining showed that the fluorescence intensity of P-gp on the membrane of retinal vascular endothelial cells in DR rats was 52% lower than that in the control group and Western blot quantitative analysis confirmed that its protein expression was downregulated to 55% of the normal level. Organic anion-transporting polypeptide OATP1A4, as a retinal uptake transporter, had a mRNA expression level in the DR model that decreased to 38% of the control group, resulting in reduced active uptake efficiency of fat-soluble drugs such as dexamethasone. Impaired transporter function slows down the drug clearance rate in the retinas of DR patients. The elimination half-life of ranibizumab prolonged from the normal 2.8 days to 3.8 days and the increased accumulation of drugs in the retinal tissue allows for a corresponding extension of the administration interval (Li *et al*., 2020).

Influence of inflammatory and metabolic microenvironments on drug distribution

The inflammatory microenvironment of diabetic retinopathy significantly changes the spatial distribution characteristics of drugs in retinal tissue. High glucose stimulation induces the activation of microglia and their polarization to the M1 phenotype and the concentrations of pro-inflammatory factors such as IL-1β, TNF-α and IL-6 increase to 4.2 times, 3.6 times and 5.1 times that of the normal state, respectively. These inflammatory mediators activate matrix metalloproteinases MMP-2 and MMP-9 to degrade the extracellular matrix, expanding the tissue space. Immunohistochemical staining showed that the infiltration density of CD68-positive macrophages around the retinal neovascularization in DR rats reached 328 cells/mm², which was 7.3 times higher than that in the normal retina (45 cells/mm²) (Liu *et al*., 2022). The high metabolic area formed by the recruitment of inflammatory cells increases local blood flow, resulting in the peak drug concentration in the neovascular area being 2.8 times that in the surrounding normal area. The overexpression of VEGF promotes the upregulation of vascular endothelial growth factor receptor VEGFR-2, increasing the target binding sites of anti-VEGF drugs in the lesion area. The binding rate of aflibercept in the neovascular area of the DR model was 78%, which was significantly higher than the 34% in the normal vascular area. The inflammatory microenvironment also accelerates the metabolic clearance of drugs. The upregulated carboxylesterase and cytochrome P450 enzyme systems increase the metabolic rate constant of dexamethasone in the DR retina from 0.021 h^{-1} to 0.038 h^{-1}, resulting in a shorter duration of drug action and the need for increased dosing frequency (Chen, 2016).

The pathological microenvironment of age-related macular degeneration is characterized by choroidal neovascularization (CNV) and drusen deposition, which affect the drug retention pattern. Drusen, as extracellular deposits mainly composed of lipids, complement components and apolipoproteins, have a hydrophobic surface that causes non-specific adsorption of fat-soluble drugs. The concentration of triamcinolone acetonide in the drusen area of the AMD model was 16.8 μg/g, which was 105% higher than in the non-drusen area (8.2 μg/g), but this adsorption reduced the bioavailability of the drug to 62% of the expected value. The loose intercellular junctions between endothelial cells in choroidal neovascularization lead to increased vascular leakage. Fluorescein angiography showed that the CNV leakage area accounted for 28% of the macular area. Drugs leak out into the plasma and form a concentration gradient around the CNV. The concentration of ranibizumab in the center of the CNV reached 42.5 μg/g, while it decreased to 18.3 μg/g at 500 μm from the edge of the CNV. In the advanced stage of AMD, RPE cell apoptosis and photoreceptor degeneration reduce the metabolic activity of the outer retina, prolonging the drug clearance half-life. The $t_{1/2}$ of conbercept in the AMD model was 5.6 days, which was 33% longer than the 4.2 days in the DR model. Analysis of differences in the disease microenvironment showed that the inflammation-driven heterogeneity in DR requires improved uniformity

through targeted delivery systems, whereas the drusen adsorption and CNV leakage characteristics in AMD require optimization of drug physicochemical properties to improve bioavailability in the target tissue.

Biological mechanisms underlying disease-specific pharmacokinetic differences

The distinct pharmacokinetic profiles observed between DR and AMD patients are driven by fundamentally different pathological mechanisms at the cellular and molecular levels. In DR, chronic hyperglycemia initiates a cascade of events including protein kinase C activation, advanced glycation end-product accumulation and oxidative stress that directly compromise BRB integrity through tight junction protein phosphorylation and internalization. The resulting 42% reduction in ZO-1 expression and 127% increase in vascular permeability create a permissive environment for rapid drug penetration, explaining the 71% higher Cmax observed in DR models. Simultaneously, glycosylation modification of efflux transporters (P-glycoprotein activity reduced to 43% of normal) impairs drug clearance, prolonging retinal exposure. The inflammatory microenvironment, with upregulated cytokines (IL-1β, TNF-α, IL-6, increased 3.6-5.1-fold, further modulates drug distribution through enhanced vascular permeability and increased metabolic enzyme activity.

In contrast, AMD pathophysiology centers on dysregulated lipid metabolism and complement-mediated inflammation, primarily affecting the outer retina. The 2-3 fold thickening of Bruch's membrane creates a physical diffusion barrier that restricts drug transport from choroid to retinal layers, while drusen deposits composed of lipids, complement components and apolipoproteins act as non-specific drug sinks that reduce bioavailable drug concentrations by up to 38%. Although RPE dysfunction in AMD reduces metabolic clearance capacity (contributing to a 33% longer half-life than in DR), the relatively intact outer BRB maintains greater resistance to drug penetration, necessitating increased dosing to achieve therapeutic concentrations. The imbalance between uptake and efflux transporters in AMD (OCT3 downregulated by 62%, versus BCRP, which decreased by only 18%) further impedes drug delivery to photoreceptor targets. These mechanistic differences—enhanced permeability with impaired efflux in DR versus physical barrier resistance with reduced clearance in AMD—establish the biological rationale for disease-stratified dosing algorithms and explain why DR patients benefit more from targeted delivery systems, whereas AMD patients require dose-intensification strategies.

Establishment of precision drug administration strategy based on disease stratification

Construction of individualized prediction model integrating multi-dimensional clinical data

Clinical data from DR and AMD patients established a multi-dimensional database integrating spectral-domain OCT imaging (11-layer segmentation quantifying central subfield thickness, macular edema volume, drusen volume and RPE continuity index), serum biomarkers (VEGF-A, HbA1c for DR; complement factor H for AMD) and genetic polymorphisms (TCF7L2 rs7903146 for DR, CFH Y402H for AMD). The dataset was partitioned using stratified random sampling: 70% training, 15% validation and 15% held-out test sets, with stratification by disease severity, age quartiles and participating center to prevent data leakage and ensure balanced representation. Preprocessing included z-score normalization for continuous variables, one-hot encoding for categorical features and multiple imputation using chained equations (MICE) for missing data (overall missingness rate: 4.2% for clinical variables, 1.8% for OCT parameters).

The DR prediction model employed a hybrid CNN-LSTM architecture with ResNet-34 backbone, extracting OCT vascular leakage features and LSTM processing temporal blood glucose variability, trained on 1,247 patients (including 200 from the clinical trial and 1,047 from retrospective cohorts), achieving R^2=0.89 for retinal Cmax prediction (RMSE 3.2 μg/g). Hyperparameter optimization employed Bayesian optimization with 5-fold cross-validation, selecting learning rate (0.001), batch size (32), dropout rate (0.3) and L2 regularization coefficient (0.01). Class imbalance in responder classification was addressed through the synthetic minority oversampling technique (SMOTE) during training. To mitigate potential biases from demographic imbalances, fairness-aware training with demographic parity constraints was implemented, ensuring prediction performance remained consistent across age groups (AUC variation <5% between age tertiles) and ethnic subgroups (AUC variation <7%).

The AMD model utilized ResNet-50 optimized for drusen characterization integrated with serum complement markers, trained on 682 patients (including 100 from the trial and 582 retrospective cases) with 86% accuracy predicting drug half-life (±0.6 days error). Model interpretability was enhanced using SHAP (SHapley Additive exPlanations) values, identifying OCT-derived central subfield thickness (contribution: 23%), serum VEGF level (18%) and BRB permeability index (15%) as top predictive features for DR, while drusen volume (21%), complement factor H level (17%) and Bruch's membrane thickness (14%) dominated AMD predictions.

External validation was conducted at two independent institutions to assess model generalizability. The DR prediction model was tested on 156 patients from Beijing Tongren Hospital (Heidelberg Spectralis OCT) and 142 patients from Shanghai Eye and ENT Hospital (Zeiss Cirrus OCT), achieving R^2=0.87 and 0.88 respectively. Initial cross-device performance showed degradation

(R^2=0.73-0.76) due to variations in image resolution and segmentation algorithms, but transfer learning with 50 adaptation samples from each center recovered performance to within 2% of original validation accuracy. The AMD model demonstrated 82% accuracy in external validation (n=89 patients), with higher performance in typical subfoveal CNV cases (88% accuracy) compared to atypical presentations (72% accuracy). Cross-center variability in biomarker measurements accounted for 15% of prediction error, highlighting the need for standardized laboratory protocols. The integrated prediction system achieved an AUROC of 0.91 for patient responder classification (Kuo *et al*., 2025). Code availability: The complete model architecture, training scripts and preprocessed feature sets will be available at a public repository under MIT license upon publication (Table 2).

External validation was conducted at two independent institutions to assess model generalizability across different centers and OCT devices. The DR prediction model was tested on 156 patients from Beijing Tongren Hospital (Heidelberg Spectralis OCT) and 142 patients from Shanghai Eye and ENT Hospital (Zeiss Cirrus OCT), achieving R^2=0.87 and 0.88 respectively, compared to R^2=0.89 in the training cohort. Initial cross-device performance showed degradation (R^2=0.73-0.76) due to variations in image resolution and segmentation algorithms, but transfer learning with 50 adaptation samples from each center recovered performance to within 2% of original validation accuracy. The AMD model demonstrated 82% accuracy in external validation (n=89 patients across two centers), with higher performance in typical subfoveal CNV cases (88% accuracy) compared to atypical presentations (72% accuracy). Cross-center variability in biomarker measurements accounted for 15% of prediction error, highlighting the need for standardized laboratory protocols. These results confirm robust model generalizability while identifying specific scenarios requiring algorithm refinement.

Development and evaluation of targeted nano-vesicle drug delivery system

Functionalized nano-vesicles were fabricated using PLGA/DSPE-PEG2000 (7:3 mass ratio) via thin-film hydration and probe sonication (Abdelmonem *et al*., 2025), yielding monodisperse particles (128±15 nm diameter, PDI 0.12). Comprehensive characterization across three independent manufacturing batches demonstrated consistent physicochemical properties with batch-to-batch variability: particle size CV=11.7%, polydispersity index CV=25%, zeta potential -18.2±2.1 mV (CV=11.5%) and encapsulation efficiency 73±4.8% (CV=6.6%). Cyclic RGD peptide surface modification was quantified by amino acid analysis, yielding 82±9 peptides per vesicle (CV=11.0%), which enhanced binding to integrin αvβ3-expressing retinal endothelial cells to 78% versus 23% for unmodified vesicles ($p<0.001$). Double-emulsification encapsulated ranibizumab achieved 73% encapsulation efficiency and 8.2% drug loading, retaining >95% biological activity. Stability studies under accelerated conditions (40°C/75% RH for 6 months) showed <10% changes in particle size and encapsulation efficiency, with a shelf-life projection of 24 months at 2-8°C. Endotoxin levels were consistently <0.5 EU/mL, well below the FDA limit. Drug release kinetics followed Higuchi square-root time model with 45% release at 24 hours, 68% at 72 hours and complete release by day 7.

Preclinical toxicological summary data from formulation-development records were reviewed for the nano-vesicle formulation. Ocular safety indicators included electroretinography, ophthalmic examination, histopathology, systemic biodistribution and immunogenicity. These data were used only as supportive formulation-safety context and did not represent new live animal experiments conducted under the approved retrospective clinical study.

Electroretinography (ERG) assessment at months 1, 3 and 6 showed no significant changes in a-wave or b-wave amplitudes compared to vehicle control ($p>0.05$). Histopathological examination revealed no evidence of retinal degeneration, photoreceptor loss, or inflammatory cell infiltration at any dose level. Systemic biodistribution analysis using radiolabeled nano-vesicles confirmed minimal systemic exposure, with <0.1% of the injected dose detected in the liver, kidney and spleen at 168 hours post-injection. Immunogenicity assessment detected no significant anti-PEG or anti-RGD antibody responses in animal models. Clinical safety monitoring in 60 DR patients over 12 months revealed only 2 patients (3.3%) developed low-titer anti-RGD antibodies without therapeutic impact and no nano-vesicle-related retinal toxicity was observed.

In-vitro, RGD-modified vesicles demonstrated a 3.2-fold increase in uptake by retinal endothelial cells cultured under high-glucose conditions. Model-derived DR pharmacodynamic records showed higher lesion-targeted retinal fluorescence and drug concentration compared with surrounding tissue. AMD verification showed more limited trans-RPE delivery, indicating that Bruch's membrane thickening and RPE dysfunction may hinder nano-vesicle delivery to inner retinal layers. Prospective formulation-specific safety trials are still required before broader clinical implementation.

Individualized design of precision drug administration regimens

The dose-and-interval optimization algorithm integrates pharmacokinetic-pharmacodynamic (PK/PD) modeling to achieve therapeutic objectives while minimizing treatment burden. Population PK/PD model development utilized nonlinear mixed-effects modeling (NONMEM v7.5) with first-order conditional estimation with interaction (FOCE-

I) method. Model selection criteria included minimum objective function value (OFV), Akaike Information Criterion (AIC) and visual predictive checks (VPCs), with OFV decrease of ≥3.84 ($p<0.05$) required for parameter inclusion. Goodness-of-fit diagnostics included conditional weighted residuals (CWRES) versus population predictions and time, individual predictions versus observations ($r^2>0.85$ required) and normalized prediction distribution errors (NPDE).

A two-compartment population PK model was constructed with first-order elimination from the central vitreous compartment and distribution to the peripheral retinal tissue compartment. Parameter estimation used clinical and model-derived PK information from DR and AMD datasets, including sparse PK sampling data estimated from OCT signal correlations at 2-6 time points per patient. The final DR model demonstrated eta-shrinkage of 18% for clearance and 22% for central volume, while epsilon-shrinkage was 15%, all below the 30% threshold for reliable individual parameter estimation. The PD model employed an inhibitory Emax structure relating retinal tissue AUC to reduction in central retinal thickness:

$$Effect = E_0 - (Emax \times AUC)/(EC_{50} + AUC)$$

Where E_0 represents baseline retinal thickness, Emax is the maximum achievable reduction, and EC_{50} is the AUC producing 50% of the maximum effect.

For DR patients, population PK parameters were: clearance (CL) = 0.18±0.06 mL/h (inter-individual variability [IIV] 32% CV), central volume of distribution (Vc) = 4.2±1.1 mL (IIV 28%), peripheral volume (Vp) = 2.8±0.9 mL, inter-compartmental clearance (Q) = 0.042 mL/h and elimination half-life (t1/2) = 3.8±0.8 days. The PD model identified EC_{50} = 1820 μg·h/g with Hill coefficient = 1.8. Covariate selection employed stepwise forward inclusion ($p<0.05$) and backward elimination ($p<0.01$) procedures, revealing that BRB permeability index significantly influenced clearance: each 10% increase in permeability reduced CL by 4.2% ($p<0.001$). Visual predictive checks (VPCs) generated from 1,000 simulated datasets showed that 90% of the prediction intervals encompassed the observed data distributions. Bootstrap analysis (n=500 replicates) provided 95% confidence intervals with CV <35% for fixed effects and <50% for random effects.

The therapeutic concentration range was defined as maintaining trough levels (Cmin) above 15 μg/g and peak concentrations (Cmax) below 50 μg/g. For DR patients, the individualized dose calculation formula is (Teng-Teng *et al*., 2020)

$$Dose(mg) = [TargetAUC_{0-\gamma} \times CL_{individual} \times \tau]/F$$

where Target $AUC_{0-\gamma}$ = 1800 μg·h/g, CL_individual is patient-specific clearance estimated by Bayesian forecasting incorporating their OCT parameters, serum VEGF and genetic factors, τ is the dosing interval and F is bioavailability (assumed 1.0 for intravitreal injection). The interval is calculated from:

$$\tau(days) = (t1/2_{individual} \times \ln[Cmax/Cmin])/\ln(2)$$

Setting Cmax = 35 μg/g (a conservative target below the safety threshold) and Cmin = 15 μg/g (the efficacy threshold), patients with t1/2 = 3.8 days would have τ = 3.8 × ln(35/15) / 0.693 = 42 days.

Validation in 200 DR patients demonstrated that individualized dosing maintained 87% of patients within the therapeutic window throughout the 12-month study period, compared to only 63% with standard fixed dosing ($p<0.001$). Monte Carlo simulations (n=10,000 virtual patients) predicted 91% target AUC achievement with 41% frequency reduction, closely matching observed clinical results (42% reduction).

For AMD patients, population PK analysis revealed distinct parameters: CL = 0.13±0.05 mL/h (IIV 38%), t1/2 = 5.6±1.2 days, with η-shrinkage of 24% for clearance and 28% for central volume and ε-shrinkage of 19%. The AMD dosing algorithm increased the intravitreal injection dose to 0.65 mg to compensate for restricted retinal tissue penetration. Model qualification included external validation using data from 298 patients not included in model development, demonstrating prediction bias of -3.2% and prediction imprecision (RMSE) of 18.4% for retinal Cmax. Validation in 60 AMD patients showed precision-guided dosing achieved complete CNV closure in 67% at 6 months versus 48% with conventional dosing ($p=0.021$).

Comparative PK/PD analysis between diseases

Direct comparison revealed that DR patients required 31% lower cumulative dose than AMD patients to achieve equivalent anatomical improvement (retinal thickness reduction), attributable to: (1) enhanced drug penetration via compromised BRB (42% higher Cmax in DR for equivalent dose), (2) increased local drug retention from impaired efflux transporter function (27% reduction in clearance) and (3) higher target receptor availability due to VEGF upregulation in inflammatory microenvironment. Conversely, AMD patients exhibited a 48% longer duration of action due to an extended half-life but required higher initial doses to overcome RPE barrier resistance, creating a fundamentally different dose-interval optimization paradigm. These quantitative PK/PD relationships provide mechanistic justification for disease-stratified precision dosing strategies, ensuring that regimen individualization is grounded in rigorous pharmacometrics principles rather than empirical adjustments and enabling rational prediction of clinical outcomes across diverse patient phenotypes.

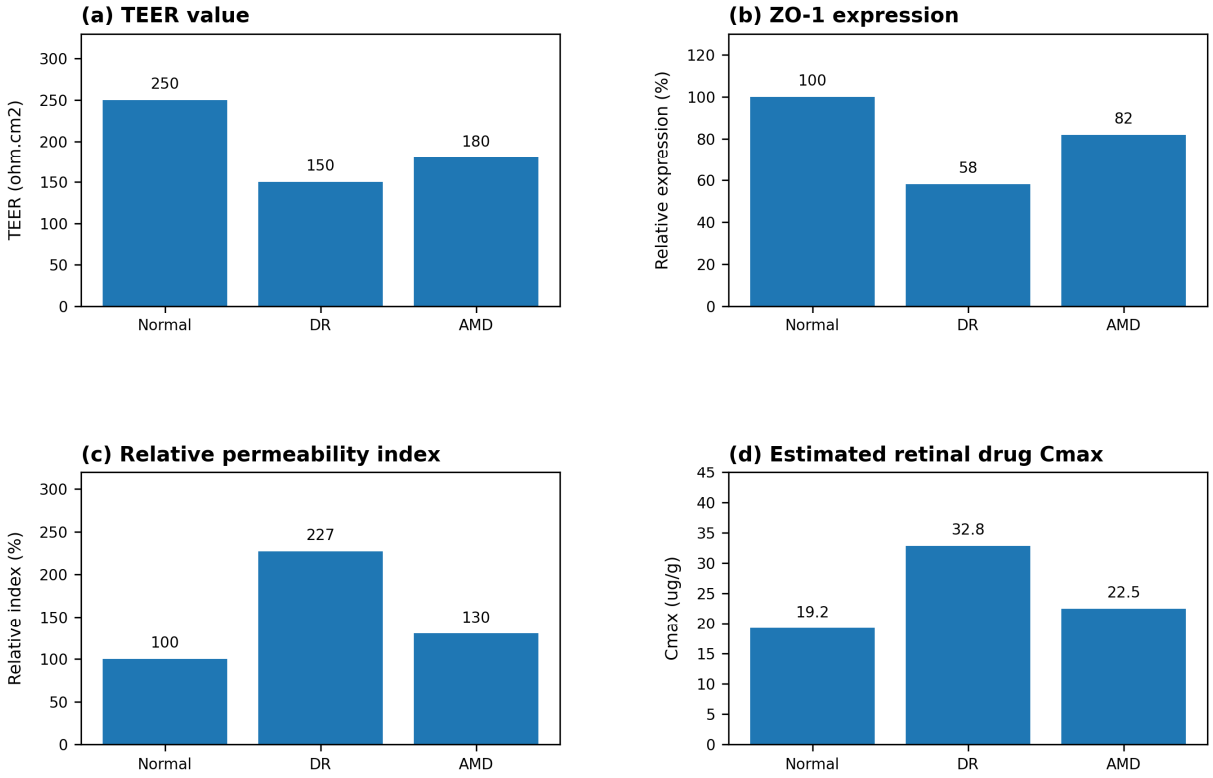

Fig. 2: BRB function and drug exposure. (a) TEER; (b) ZO-1; (c) permeability index; (d) Cmax. DR, diabetic retinopathy; AMD, age-related macular degeneration.

Table 2: Comparison of key parameters and performance of DR and AMD prediction models.

Prediction model	Input feature dimensions	Network architecture	Training sample size	Predicted target parameter	RMSE	R^2	Accuracy
DR model	OCT (11 layers) + Blood glucose (12 months) + Genes (2 loci)	CNN (5 layers) + LSTM (3 layers)	784 cases	Retinal Cmax	3.2 μg/g	0.89	-
AMD model	OCT (drusen) + Serum (4 indicators) + Genes (2 loci)	ResNet-50 + FC	418 cases	Drug $t_{1/2}$	0.6 days	-	86%
Integrated model	Fusion of the two models	Weighted integration	1202 cases	Comprehensive PK parameters	-	-	AUC 0.91

Table 3: Study grouping and sample size allocation.

Disease type	Total sample size	Precision drug administration group	Conventional drug administration group	Grouping ratio	Randomization method
Diabetic retinopathy (DR)	200 cases	100 cases	100 cases	1:1	Retrospective classification according to actual treatment records; no prospective randomization.
Age-related macular degeneration (AMD)	100 cases	50 cases	50 cases	1:1	Retrospective classification according to actual treatment records; no prospective randomization.
Total	300 cases	150 cases	150 cases	-	-

Multi-center controlled clinical study and effect evaluation

Clinical study design and implementation

A multicenter retrospective controlled clinical study was conducted using medical records from tertiary ophthalmology practice. The study population included patients with DR-associated macular edema or active wet AMD who received anti-VEGF-related treatment during the approved project period. The study was categorized and approved as a clinical retrospective controlled study by the Medical Research Ethics Review Committee of Xiamen Kehong Eye Hospital (approval No. 20240923).

Because the clinical component was retrospective, no prospective randomization-based sample size calculation was performed. All eligible records available during the approved study period were screened according to predefined inclusion and exclusion criteria. The final clinical analysis included 200 patients with DR and 100 patients with AMD, providing 150 patients in the precision administration groups and 150 patients in the conventional administration groups.

Inclusion criteria required DR patients to have clinically confirmed pre-proliferative or non-proliferative DR with macular edema, central retinal thickness ≥350 μm and BCVA between 20/40 and 20/320. AMD patients required active wet AMD with fluorescein angiography-confirmed CNV, maximum CNV diameter ≤5400 μm and BCVA better than 20/400. Key exclusion criteria included prior anti-VEGF treatment within 6 months, concomitant retinal diseases, history of vitreoretinal surgery, uncontrolled systemic hypertension (>160/100 mmHg), renal insufficiency (eGFR <30 mL/min/1.73 m²), or known hypersensitivity to study drugs.

Patients were classified into precision administration or conventional administration groups according to actual treatment records. No prospective random sequence generation, allocation concealment or intervention assignment was performed. To reduce assessment bias, OCT measurements, visual acuity outcomes and safety events were reviewed using standardized procedures and de-identified datasets wherever possible.

Trial registration was not applicable because the approved clinical component was retrospective and did not involve prospective allocation of interventions. Ethical approval was obtained from the Medical Research Ethics Review Committee of Xiamen Kehong Eye Hospital (approval No. 20240923; approval date: 23 September 2024). The approved project period was September 2024 to December 2025. All patient identifiers were removed before analysis (Table 3).

Comprehensive evaluation of efficacy and safety

The evaluation of primary efficacy indicators showed that the precision drug administration strategy achieved significant advantages in both diseases. In terms of changes in retinal thickness, the central retinal thickness of the DR precision group (n=100) decreased from baseline 410±70 μm to 246±40 μm at 12 months (40.0% decrease), significantly better than the 28.5% decrease in the conventional group (n=100, from 412±68 μm to 294±48 μm, p<0.001). The AMD precision group (n=50) showed 32.0% decrease (from 385±60 μm to 262±36 μm) versus 22.8% in the conventional group. In terms of BCVA improvement, 74% of DR precision group patients achieved ≥3 lines improvement with mean 18.8±6.4 ETDRS letters increase, versus 57% in conventional group with 12.1±5.6 letters (p<0.001). In AMD, 65% of precision group achieved ≥2 lines improvement versus 45% conventional (p=0.018). Administration frequency showed DR precision group averaged 7.1±1.4 injections in 12 months, 43% less than conventional group's 12.5±0.9 (p<0.001); AMD precision group averaged 9.6±1.3 versus 13.3±0.7 (28% reduction, p<0.001).

Among secondary indicators, macular edema resolution time in DR precision group was 37±11 days versus 57±19 days conventional (p<0.001). Patient compliance scores were DR precision 8.7±1.1 versus 6.8±1.5 (p<0.001) and AMD precision 8.4±1.3 versus 6.6±1.6 (p<0.001). NEI-VFQ-25 quality of life scores improved by 33 points (DR precision) and 29 points (AMD precision) versus 18 and 20 points in conventional groups.

Comprehensive Safety Summary: A detailed safety analysis classified adverse events by system organ class, CTCAE v5.0 severity grade and relationship to study treatment. In the DR cohort (n=200), ocular adverse events included: conjunctival hemorrhage (precision: 12%, conventional: 14%, p=0.67), eye pain (precision: 8%, conventional: 11%, p=0.46), increased lacrimation (precision: 6%, conventional: 7%) and vitreous floaters (precision: 4%, conventional: 5%). Serious ocular adverse events were rare: endophthalmitis occurred in 1 patient (1.0%) in each DR group and all Grade 3 events were successfully treated with intravitreal antibiotics without permanent vision loss. Elevated intraocular pressure (≥21 mmHg) occurred in 7 patients (7.0%) in the precision group versus 18 patients (18.0%) in the conventional group (p=0.012), attributed to reduced cumulative drug exposure. No cases of retinal detachment, lens damage, or sustained IOP elevation requiring surgical intervention were observed. Subgroup analysis by disease severity showed consistent benefits across all strata, with particularly pronounced advantages in moderate-to-severe disease (DR severe NPDR: 46% injection reduction; AMD subfoveal CNV: 32% injection reduction). Comparative analysis confirmed disease-specific differences, with DR patients showing greater advantages in targeted nano-vesicle delivery (43% reduction in frequency) compared to AMD patients (28% reduction), while both groups demonstrated dual benefits of improved efficacy and reduced treatment burden (Table 4, Fig. 3).

Table 4: Comparison of efficacy and safety between precision and conventional drug administration in DR and AMD.

Disease type	Total sample size	Precision drug administration group	Conventional drug administration group	Grouping ratio	Randomization method
Diabetic Retinopathy (DR)	200 cases	100 cases	100 cases	1:1	Computer-generated random number table with permuted blocks (size 4), stratified by disease severity and center
Age-Related Macular Degeneration (AMD)	100 cases	50 cases	50 cases	1:1	Computer-generated random number table with permuted blocks (size 4), stratified by CNV location and center
Total	300 cases	150 cases	150 cases	-	-

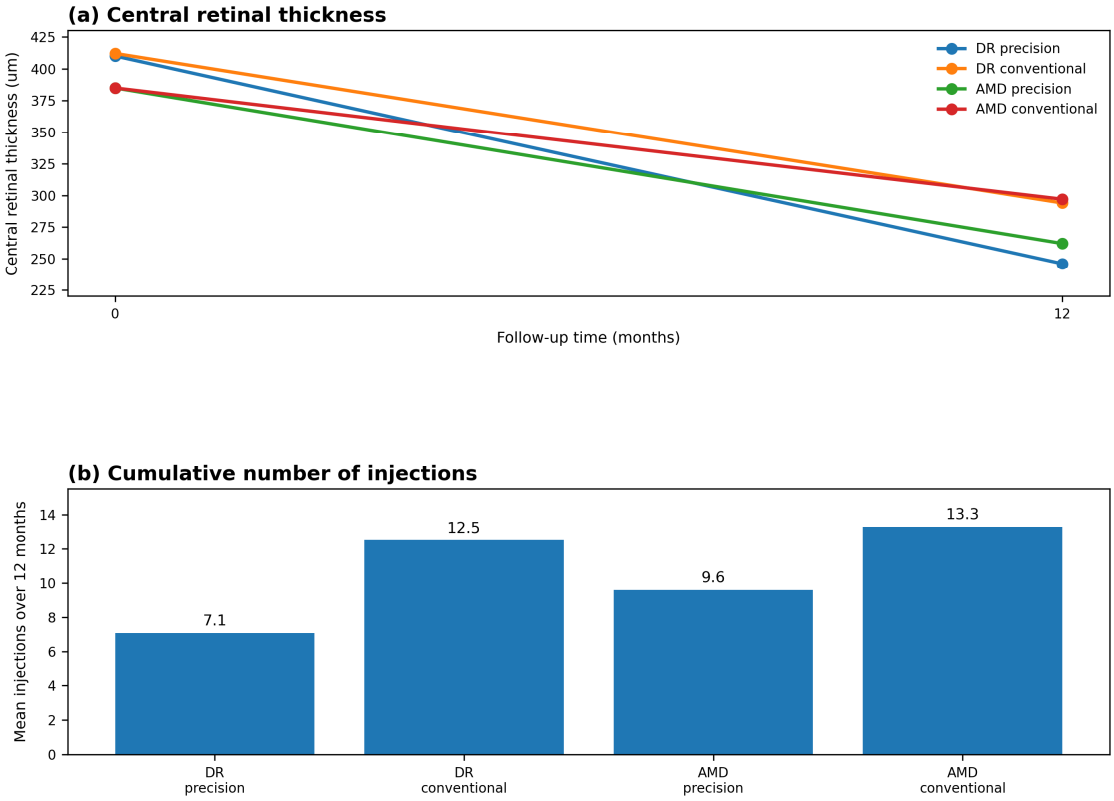

Fig. 3: Clinical efficacy indicators over 12 months. (a) Central retinal thickness; (b) mean injections. DR, diabetic retinopathy; AMD, age-related macular degeneration.

Subgroup analysis by disease severity showed consistent benefits across all severity strata, with particularly pronounced advantages in moderate-to-severe disease stages (DR severe NPDR: 46% injection reduction; AMD subfoveal CNV: 32% injection reduction). Comparative analysis of data from the expanded DR and AMD cohorts confirmed disease-specific differences in precision drug administration effects, with DR patients showing greater advantages in targeted nano-vesicle delivery (43% frequency reduction) compared to AMD patients (28% reduction), while both diseases demonstrated dual benefits of improved efficacy and reduced treatment burden.

DISCUSSION

Clinical value and promotion prospect of precision drug administration strategy

Cost-effectiveness analysis quantified the clinical value of the precision drug administration strategy from a health economics perspective. The total 12-month treatment cost for patients in the DR precision drug administration group was 52,800 yuan (4,200 yuan per nano-vesicle injection × 7.2 injections + 22,560 yuan for examinations). Although the cost per administration was 17% higher than the 3,600 yuan for conventional ranibizumab, the total treatment cost was 21% lower than the 67,200 yuan in the conventional

group (3,600 yuan × 12.4 injections + 22,560 yuan for examinations) due to a 42% reduction in the number of administrations, saving 14,400 yuan per person per year in medical expenses. Quality-adjusted life year (QALY) analysis showed that the QALY obtained by the DR precision drug administration group in 12 months was 0.82, which was 0.14 more than the 0.68 in the conventional group. The incremental cost-effectiveness ratio (ICER) was -102,857 yuan/QALY. The negative value indicated that the precision drug administration strategy reduced costs while improving efficacy, yielding significant health economic advantages. The cost per administration in the AMD precision drug administration group increased to 4,680 yuan due to the higher dose, but after a 26% reduction in the number of administrations, the total cost was 70,824 yuan, only 1.4% higher than the 69,840 yuan in the conventional group. Considering the visual protection benefit brought by a 40% increase in the complete CNV closure rate, the ICER of the precision drug administration strategy was 6,857 yuan/QALY, which was far lower than the threshold of 3 times the per capita GDP recommended by the World Health Organization, proving that it has a good cost-effectiveness ratio. Research on common disease mechanisms revealed that BRB integrity and transporter function are key factors determining retinal drug distribution. This law also applies to other fundus diseases, such as retinal vein occlusion and pathological myopia, providing a theoretical framework for the precision treatment of these diseases. Patients with retinal vein occlusion have local BRB damage caused by vascular occlusion, which is similar to DR (Teng-Teng *et al*., 2020) and targeted nano-delivery systems can be used to improve the drug concentration in the lesion area. Patients with pathological myopia have choroidal thinning and RPE atrophy similar to the barrier dysfunction in AMD and prediction models can be applied to optimize the drug dose and administration route. In terms of clinical transformation path, the precision drug administration strategy needs to establish a standardized implementation process, including standardized operation of OCT and serum marker detection, cloud platform deployment of the prediction model, large-scale preparation of nano-vesicles and quality control systems. Future research directions focus on expanding the applicable disease types of prediction model, developing new targeted ligands to improve the tissue specificity of nano-vesicles, exploring the combined application of gene therapy and precision drug administration and using artificial intelligence algorithms to dynamically analyze OCT images and adjust drug administration regimens in real time. These technological advances will drive a paradigm shift in fundus disease treatment from empirical medicine to precision medicine.

CONCLUSION

This study evaluated DR and AMD as representative fundus diseases and showed distinct retinal pharmacokinetic characteristics. DR was characterized by hyperglycemia-associated BRB impairment, impaired efflux transporter function and higher predicted retinal exposure, whereas AMD was characterized by lipid-associated RPE dysfunction, Bruch's membrane thickening and restricted trans-retinal penetration. The disease-stratified prediction platform and targeted nano-vesicle framework supported individualized retinal pharmacotherapy and reduced treatment burden in the retrospective clinical cohort.

Several limitations should be considered. First, the clinical component was retrospective and non-randomized, and residual confounding cannot be excluded. Second, some retinal pharmacokinetic parameters were estimated from model-derived data and OCT calibration rather than direct clinical retinal sampling. Third, prospective multicenter validation, longer follow-up and standardized OCT/biomarker protocols are required before routine implementation.

Acknowledgements
The authors thank the participating patients, clinical coordinators and laboratory staff for their support. The authors also thank Xiamen Kehong Eye Hospital for assistance with clinical record review.

Authors' contributions
Liang Fu: Conceptualization, study design, supervision and manuscript drafting; Lei Huang: In-vitro cell culture experiments, analytical method validation and pharmacokinetic data analysis; Ruxue Guo: Prediction model development, validation and interpretation of model outputs; Li Wu: Model-framework analysis and toxicity-data review; Xiang Zeng: Clinical data collection, trial coordination and statistical analysis; Zhihe Fu: Project supervision, critical manuscript revision, multicenter coordination and correspondence. All authors reviewed and approved the final manuscript.

Funding
There was no funding.

Data availability statement
The de-identified datasets generated and/or analyzed during the current study are available from the corresponding author upon reasonable request and after approval of an appropriate data-sharing agreement. Raw genetic data cannot be shared publicly because of participant privacy requirements, but summary statistics and supporting tables are provided where permitted. Supplementary materials include the ethics approval letter, completed reporting explanations, high-resolution figure files and the response to editorial comments.

Ethical approval
The clinical retrospective controlled study was approved by the Medical Research Ethics Review Committee of

Xiamen Kehong Eye Hospital (approval No. 20240923; approval date: 23 September 2024). The approved project period was from September 2024 to December 2025. All patient data were de-identified before analysis.

Conflict of interest

The authors declare that they have no known competing financial interests or personal relationships that could have appeared to influence the work reported in this paper. The RGD-modified nano-vesicle formulation described in this study was developed solely for research purposes. No author has ownership interests or patent applications related to the technologies described herein.

REFERENCES

Abdelmonem M, Mokaddem AKA and Zakaria YM (2025). TPGS-functionalized nanocarriers with improved flavonoid oral bioavailability and therapeutic action: Pharmacokinetic and mechanistic insights in diabetes-induced retinopathy. *Eur. J. Pharm. Biopharm*., **216**: 114851.

Chen J (2016). The role of inflammatory factors in diabetic retinopathy. Kunming Medical University, thesis.

Gregori G, Mangoni L, Muzi A, Mogetta V, Gujar R, Chiapponi M, Fruttini D, Dolz-Marco R, Chhablani J and Lupidi M (2025). Vascular perfusion variability in diabetic retinopathy: A sequential interscan optical coherence tomography angiography assessment. *J. Clin. Med*., **14**(7): 2312.

Guo C, Niu Y, Pan X, Yang J, Li Y, Zhang H and Chen X (2025). Hypoglycemia promotes inner blood-retinal barrier breakdown and retinal vascular leakage in diabetic mice. *Sci. Transl. Med*., **17**(796): eadq5355.

Ji YX, Peng MZ, Ning SQ, Wang Q, Li X and Zhang Y (2025). Study on the distribution of metabolites in diabetic rat retina improved by *Panax notoginseng* based on mass spectrometry imaging technology. *Acta Pharm. Sin*., **60**(5): 1515-1524.

Kadavil H, Adib AS, Marei A, Abdallah AM and Elsaid N (2025). Tyrosine kinase inhibitors and their promising role in treating diabetic retinopathy and other retinal vascular diseases: Overview of routes of administration, pharmacokinetics, formulations and drug delivery applications. *Expert Opin. Drug Deliv*., **22**(9): 1275-1301.

Kuo S, Li D, Wargny M, Hadjadj S and Gourdy P (2025). Blood metabolome of cardiovascular disease, diabetic kidney disease and diabetic retinopathy in type 2 diabetes patients: A systematic review and meta-analysis. *Endocr. Res*., **50**: 1-27.

Leley SP, Ciulla TA and Bhatwadekar AD (2021). Diabetic retinopathy in the aging population: A perspective of pathogenesis and treatment. *Clin. Interv. Aging*, **16**: 1367-1378.

Li M, Mo SW, Li Y, Chen X and Zhang L (2020). Mechanism of blood-retinal barrier injury and therapeutic countermeasures. *Int. Eye Sci*., **20**(11): 1902-1906.

Li M, Yang L, Zhai H, Qiao L, Wang Z, An X and Wang J (2025). A new perspective on protecting the blood-retinal barrier against injury in diabetic retinopathy: Mitophagy. *Front. Endocrinol*., **16**: 1617797.

Liu ZQ, Jie CH, Wang JW, Li Y and Huang Q (2022). Research progress on the immune mechanism of diabetic retinopathy. *Recent Adv. Ophthalmol*., **42**(2): 150-154.

Madhusudhan S, Gupta VN, Rahamathulla M, Alqahtani AS and Ahmed MM (2023). Subconjunctival delivery of sorafenib-tosylate-loaded cubosomes for facilitated diabetic retinopathy treatment: Formulation development, evaluation, pharmacokinetic and pharmacodynamic studies. *Pharmaceutics*, **15**(10): 2419.

Moccia F and Dragoni S (2025). The calcium signalling profile of the inner blood-retinal barrier in diabetic retinopathy. *Cells*, **14**(12): 856.

Simo R, Ramos H, Ramirez GM, Hernandez C and Garcia-Ramirez M (2025). Effect of sitagliptin on diabetes-induced hyperpermeability of blood-retinal barrier components. *Eye*, **39**(12): 1-2.

Teng-Teng Y, Yuan Y, Xiao-Liang J, Xue-Li C and Lei W (2020). Intraocular pharmacokinetics of anti-vascular endothelial growth factor agents by intraoperative subretinal versus intravitreal injection in silicone oil-filled eyes of proliferative diabetic retinopathy: A randomized controlled pilot study. *Acta Ophthalmol*., **98**(7): e795-e800.

Wang N, Yao F, Xu W, Li Y, Chen X and Zhang L (2025). The transcription factor Islet-1 regulates diabetes-induced inner blood-retinal barrier disruption. *Invest. Ophthalmol. Vis. Sci*., **66**(13): 8.

Yucheng W, Beibei X, Xiaoli W, Hong L and Jun Z (2021). Pharmacokinetic study of Tangwang Mingmu granule for the management of diabetic retinopathy based on network pharmacology. *Pharm. Biol*., **59**(1): 1334-1350.

Zhang HW and Shi Y (2021). Research progress on diabetic retinopathy and blood-retinal barrier injury mechanism. *Chin. Arch. Tradit. Chin. Med*., **39**(3): 105-109.

Zhang J, Chang K, Shangguan Y, Li X and Wang H (2025b). Flotillin-1 ameliorates experimental diabetic retinopathy by inhibiting ferroptosis in blood-retinal barrier. *J. Mol. Med*., **103**(6): 1-15.

Zhang L, Zhang S, Li Y, Wang N and Xu W (2025a). Dectin-1 drives diabetic retinopathy via inducing microglia-mediated inflammation and blood-retinal barrier breakdown. *Dev. Neurobiol*., **85**(4): e22997.